Optogenetically controlled inflammasome activation demonstrates two phases of cell swelling during pyroptosis

Julien Nadjar, Sylvain Monnier, Estelle Bastien, Anne-Laure Huber, Christiane Oddou, Léa Bardoulet, Hubert Leloup, Gabriel Ichim, Christophe Vanbelle, Bénédicte Py, et al.

Optogenetically-controlled inflammasome activation demonstrates two-step cell swelling during pyroptosis.

Julien Nadjar1*, Sylvain Monnier2*□, Estelle Bastien2, Anne-Laure Huber1, Christiane Oddou3, Léa Bardoulet1, Hubert B. Leloup1, Gabriel Ichim1, Christophe Vanbelle1, Bénédicte F. Py4, Olivier Destaing3# and Virginie Petrilli1#□.

1 CRCL, Centre de Recherche en Cancérologie de Lyon, INSERM U1052, CNRS UMR5286, Université de Lyon, Université Claude Bernard Lyon 1; Centre Léon Bérard F-69000 Lyon, France.

2 Université de Lyon, Université Claude Bernard Lyon 1, CNRS, Institut Lumière Matière, F-69622, VILLEURBANNE, France.

3 DYSAD, Institut pour l'avancée des biosciences (IAB), Centre de Recherche UGA / Inserm U 1209 / CNRS UMR 5309, France.

4 CIRI, Centre International de Recherche en Infectiologie, Université de Lyon, Inserm, U1111, Université Claude Bernard Lyon 1, CNRS, UMR5308, ENS de Lyon, F-69007, Lyon, France. *: equal contribution

#: equal contribution

□ Corresponding authors: virginie.petrilli@lyon.unicancer.fr and sylvain.monnier@univ-lyon1.fr

Inflammasomes are multiprotein platforms that control caspase-1 activation, which stimulates the inflammatory cytokines IL-1β and IL-18 and an inflammatory cell death called pyroptosis. Studying inflammasome-driven activities such as pyroptosis-induced cell swelling remains challenging because the signals that activate these complexes trigger different signaling pathways. We designed an optogenetic approach to temporally and quantitatively manipulate the exclusive activation of the inflammasome. We demonstrated that controlling light-sensitive oligomerization of the inflammasome adaptor ASC is sufficient to recapitulate the classical features of inflammasomes within minutes. Using this system, we showed that pyroptotic swelling is a two-step process. Overall, this approach offers perspectives to revisit pattern recognition receptor signaling pathways in the field of innate immunity and offers new perspectives for biophysical investigations into the intricate nature of cellular volume control and plasma membrane rupture during cell death.

Introduction

Inflammasomes are dynamic multiprotein complexes involved in innate immunity and inflammation. They form upon sensing of pathogen-associated molecular patterns (PAMPs) (for example, the bacterial toxin nigericin) or damage-associated molecular patterns (DAMPs) (for example, extracellular ATP) by a pattern recognition receptor (PRR), such as NACHT, LRR and pyrin domain containing protein 3 (NLRP3). The PRR then drives the formation of nanoclusters of apoptosis-associated speck-like containing a caspase recruitment domain (ASC) necessary to recruit and activate the cysteine protease caspase-1 (CASP1) at the complex, through their caspase recruitment domain (CARD) (*1*). Hetero-oligomerization of the inflammasome core proteins ASC and CASP1 filaments results in large membraneless structures, between 0.2-1 µm in diameter, called specks (*2*–*4*). Activated CASP1 then cleaves proinflammatory proIL-1b and proIL-18 cytokines and the gasdermin-D (GSDMD) protein to induce an inflammatory form of cell death called pyroptosis (*5*–*7*). Indeed, the resulting GSDMD N-terminus fragments self-oligomerize and are inserted into the plasma membrane (PM) to form pores contributing to IL-1b and IL-18 release, cell swelling, plasma membrane rupture (PMR) and therefore lytic cell death (*8*, *9*). Ninjurin-1 (NINJ1) acts downstream of GSDMD to execute PMR but the mechanism of action remains largely unknown (*10*). Inflammasome dysregulation results in many pathologies. For instance, mutations in NLRP3 promotes auto-inflammatory disorders such as cryopyrin-associated periodic syndrome (CAPS), and dysregulation of its activity promotes metabolic and inflammatory disorders including gouty arthritis, atherosclerosis and type 2 diabetes (*11*–*15*). The development of inhibitors of pyroptosis to treat these pathologies represents a promising field of research. Inflammasome assembly requires stimulation with PAMPs or DAMPs, which are not exclusively involved in inflammasome assembly, but also activate other PRRs and their downstream signaling pathways. NLRP3 inflammasome formation also relies on an upstream priming signal, necessary to induce the expression of pro-IL-1β and NLRP3, and for NLRP3 post-translational modifications (*16*). This priming signal originates either from inflammatory cytokines or PAMPs, such as binding of lipopolysaccharide (LPS) to the toll-like receptor 4 (TLR4). Therefore, studying the sole output of inflammasome activation and its cellular dynamics remains

challenging using classical pharmacological and genetic approaches, since signaling downstream of DAMPs or PAMPs is intricate and not limited to inflammasome formation.

Cell swelling and PMR are important features of pyroptosis, but the physical changes underlying these events are poorly understood. This is mostly due to a lack of tools for measuring biophysical parameters and inducing pyroptosis under controlled conditions. Indeed, many PAMPs or DAMPs directly affect PM permeability (for example, nigericin or ATP). Moreover, precise measurements of cell swelling are limited by available technology (*17*). To address this problem, we developed an optogenetic tool to directly control the oligomerization of the inflammasome core adaptor ASC independently of the extracellular environment. Optogenetics has been widely used in the field of neurosciences to activate neurons in a reversible manner and is continually adapted to other cellular functions dependent on the nanoclustering of sub-cellular complexes, in a controlled spatial and temporal manner (*18*–*20*). Here, to spatio-temporally manipulate inflammasome activation, we engineered a new photo-oligomerizable ASC based on the photolyase homology domain (PHD) of cryptochrome 2 (CRY2) of *Arabidopsis thaliana*. CRY2 homo-oligomerizes upon blue light stimulation. We demonstrate that simple nanoclustering of ASC upon exposure to light is sufficient to induce a complete physiological inflammasome response (*21*, *22*), which is CASP1-dependent but PAMP- and DAMP-independent. Therefore, our model represents a useful tool with many possible applications ranging from the molecular dissection of events leading to inflammasome output to the screening of specific inhibitors. Here, we used this system to study the changes in cellular volume during inflammasome-induced pyroptosis. We precisely measured cell swelling and demonstrated a two step-mediated cell swelling before plasma membrane rupture.

RESULTS

Opto-ASC assembles in specks upon classical inflammasome activation

To study the output of inflammasome assembly without interference from DAMP/PAMP priming or activating signals, we designed a lentiviral vector to express the human protein ASC coupled to CRY2 PHD and to red fluorescent protein (RFP), which we named opto-ASC (Fig. 1). We reasoned that the CRY2 PHD homo-oligomerizer should initiate ASC oligomerization upon exposure to blue light, thus mimicking its physiological engagement by a PRR such as NLRP3 (*21*, *22*). Consequently, ASC would recruit and activate CASP1 resulting in the induction of

specific canonical inflammasome-dependent responses (Fig. 1). Immortalized bone marrow-derived macrophages (iBMDMs) were transduced to stably express opto-ASC (or the relevant control opto alone) and FACS-sorted according to RFP expression in order to normalize vector expression. Expression of opto-ASC did not affect the expression of endogenous ASC or CASP1 (fig S1A and B). We initially verified that the opto-ASC behaved like the endogenous protein and would not interfere with the physiological activation of inflammasomes. To achieve this, parental cell lines and cells expressing opto-ASC were primed with LPS to induce NLRP3 and pro-IL-1β expression, and activated with the bacterial toxin nigericin to trigger the assembly of the NLRP3 inflammasome (*23*). Analysis of NLRP3 inflammasome activation by immunoblot revealed that nigericin induced CASP1 activation, in both parental and opto-ASC-expressing cells, as evidenced by the detection of cleaved CASP1 (p20), GSDMD N-terminus fragment (p30) and IL-1b (p17) in cell supernatants (fig. S1C). A small increase in the cleavage of these substrates was observed in the opto-ASC condition, likely due to a higher expression of ASC (endogenous and exogenous ASC). No spontaneous CASP1 activation was detected in resting opto-ASC-expressing cells. As a control, treatment with VX-765, a specific CASP1 inhibitor, blocked CASP1 activation in both cell lines, clearly showing that ASC over-expression did not affect the sensitivity of the inflammasome reaction (fig. S1C). Two other inhibitors were tested on opto-ASC-containing cells, Z-VAD-fmk, a pan caspase inhibitor, and YVAD-fmk a CASP1 inhibitor. Both inhibited IL-1b and CASP1 cleavage upon treatment with nigericin (fig. S1D). A hallmark of inflammasome assembly is the formation of ASC specks in the cell cytosol (*2*, *3*). Nigericin treatment induced ASC-RFP+ speck, cell swelling, loss of PM integrity, as visualized by TO-PRO-3 membrane non-permeant staining, which are features of pyroptosis (fig. S1E). We concluded that opto-ASC assembles in specks similar to endogenous ASC, and that exogenous expression of opto-ASC neither affects inflammasome activation nor induces spontaneous inflammasome responses.

Light activation of opto-ASC induces canonical inflammasome features

Next, we tested whether blue light (488 nm) activation of opto-ASC is sufficient to induce inflammasome assembly and activation in the absence of stimulation by PAMPs or DAMPs. To address this, we first determined that light stimulation induced the formation of opto-ASC specks associated with pyroptosis using confocal microscopy. As expected, upon light stimulation, we observed that opto-ASC oligomerized into specks (ASC-RFP+), which was

followed by cell swelling, loss of PM integrity and therefore cell death, as illustrated by TO-PRO-3+-stained DNA (Fig. 2A). The addition of VX-765 (CASP1 inhibitor) inhibited cell swelling and loss of membrane integrity, but not the formation of RFP+ specks, indicating that light activated opto-ASC induces pyroptosis in a CASP1-dependent manner (Fig. 2A, movies 1 & 2). We noted that ASC specks were still present 30 minutes after stimulation. As an additional control, light activation of cells expressing the opto construct alone did not display any speck nor loss of membrane integrity (Fig. 2A). Pyroptosis can be better visualized using Nanolive, a cell tomography microscope, which enables users to specifically see changes in membrane, cytosol and nuclear organizations (*24*). Opto-ASC iBMDM activated with either nigericin, ATP (a DAMP activating NLRP3), or light indicated that all treatments induced cell swelling associated with pyroptosis (see movies 3 & 4; fig. S2A). Lactate dehydrogenase (LDH) release into the supernatant upon PMR is another classical cell death marker used to quantify pyroptosis. For quantitative analysis, we activated a large population of iBMDM stably expressing opto-ASC in an incubator equipped with blue LEDs. As expected, applying light stimulation to opto-ASC-expressing cells induced specific LDH release, independently of the presence of a priming signal (LPS), whereas VX-765 inhibited it (Fig. 2B). Parental cells stimulated with light did not display an increase in cell death (fig. S2B), demonstrating that the effect observed was not due to light phototoxicity. Thus, the simple and direct activation of opto-ASC clustering with blue light was sufficient to recapitulate canonical features of pyroptosis, independently of any upstream signal.

To further ascertain that opto-ASC activation induced CASP1 activation, we quantified by ELISA the amount of IL-1b released into the supernatant in response to light stimulation. IL- 1β secretion was detected only when pyroptosis was initiated by opto-ASC activation preceded by LPS stimulation, since a priming signal is required to induce pro-IL-1β synthesis (Fig. 2C). Our synthetic strategy allowed us to uncouple the production of IL-1b from pyroptosis. Finally, light activation of opto-ASC also promoted IL-18 secretion (fig. S2C).

To demonstrate in a more direct manner that opto-ASC induced CASP1 activation, we analyzed by immunoblot whether CASP1, pro-IL-1β and GSDMD were cleaved upon exposure to light. By applying a range of light stimulations, we were able to achieve different amounts of CASP1 activation, as illustrated by the increasing amounts of cleaved IL-1b and GSDMD detected in cell supernatants and cell extracts (Fig. 2D and fig. S2D). ELISA quantification of mature IL- 1β suggested that the maximum of CASP1 activation was reached around 50 stimulations (fig.

S2E). Parental (WT) or opto-expressing cell lines used as controls did not produce any cleaved CASP1 substrate following light stimulation, nor did they induce cell death (Fig. 2D and fig. S2F and G). As expected, light-dependent CASP1 activation was prevented by VX-765 treatment, confirming the physiological functions of opto-ASC activation (Fig. 2D and fig. S2F). The different ranges of stimulation also resulted in progressive LDH release until they reached a plateau (fig. S2H). These results suggest that opto-ASC activity can be modulated by applying different patterns of light stimulation.

The activity of opto-ASC relies on inflammasome effectors

Because GSDMD is the main effector of pyroptosis, we transduced the opto-ASC construct into iBMDM *Gsdmd*-/- cells, to verify their response to inflammasome activation. Light activation promoted ASC speck formation, but we observed no cell swelling, no TO-PRO-3 staining, no LDH release, and no IL-1b secretion, unlike opto-ASC WT cells, indicating the absence of pyroptosis (Fig. 3A, fig. S2F and G). Because glycine was reported to act as a cytoprotectant by preventing PMR through NINJ1 oligomerization impairment, we tested whether it could prevent opto-ASC-induced cell lysis (*5*, *25*). Opto-ASC-expressing cells were incubated in culture medium supplemented or not with glycine. In WT opto-ASC cells, glycine treatment inhibited light-dependent LDH release, and therefore PMR, but not IL-1b which is secreted through GSDMD pores (fig. S2F and G). VX-765 was added as a positive control for CASP1 inhibition. Hence, here, light stimulation induced the formation of opto-ASC specks that leads to CASP1 activation, the subsequent release of IL-1b and pyroptosis in a GSDMD-dependent manner, recapitulating the canonical function of inflammasomes.

To further validate our synthetic strategy, we investigated whether we could induce inflammasome responses in mouse embryonic fibroblasts (MEFs) by stably expressing opto-ASC, since they are naturally inflammasome-free cells, that is, they do not express inflammasome core proteins but express effector proteins GSDMD and NINJ1 (fig. S3A-C). In this cellular environment, light stimulation was sufficient to induce autonomous opto-ASC oligomerization, as evidenced by RFP+ specks, but neither cell death (absence of TO-PRO-3 staining) nor cell swelling (Fig. 3B). CASP1 transduction in opto-ASC MEFs promoted pyroptosis as demonstrated by TO-PRO-3-positive staining and GSDMD cleavage in response to light stimulation (Fig. 3B and Fig. S3C) (*3*). The pyroptosis specificity was confirmed by cell death inhibition in the presence of VX-765 (Fig. 3B). Finally, to demonstrate that CASP1 is recruited to ASC-RFP specks, we immunostained CASP1 in MEFs and were able to detect the co-

localization of both proteins upon light stimulation (fig. S3D). These results clearly establish that opto-ASC does not have off-target effects and that we are able to uncouple IL-1b secretion from cell death. In addition, they demonstrate that it is possible to use opto-ASC in an inflammasome-deficient cellular environment and to reconstitute functional inflammasome responses. This perspective is a prerequisite to control and calibrate inflammasome assays, an essential step for investigating structure-function relationships of ASC, CASP1 or any mutants of inflammasome components.

Opto-ASC induces an all-or-nothing commitment

For screening approaches, and to characterize our tool more precisely, we tested the sensitivity of opto-ASC activation using an automated confocal microscope (Operetta CLSTM microscope) and followed cell response to different settings of stimulations by modulating laser intensity or stimulation frequencies. Here, TO-PRO-3+ cells were used as a readout of CASP1 activation over time (Fig. 4A). As a control, cells expressing only the opto construct were stimulated alongside opto-ASC-expressing cells. As expected, no cell death was detected in the cells expressing the opto construct over time (fig. S4). For data quantification, we fitted the raw data (percentage of cell death) to a sigmoid function, $f(t) = A_{max}/(1 + e^{-(t-\tau_{1/2})/dt})$ and extrapolated the percentage of dead cells at the end of the experiment (amplitude, A_{max}) and the time at which half the cells had died (inflection point, $\tau_{1/2}$) (Fig. 4B). Regarding the amplitude, increasing the intensity of light, with a fixed number of stimulations, led to an increase in the rate of cell death, as illustrated by the difference between 1%, 5% and 15% laser intensity although 1% weakly induced cell death (Fig. 4C and D). However, the inflexion point remained unchanged although the number of stimulations increased (Fig. 4E). Similarly, when using a fixed laser intensity with increasing number of stimulations, we observed an increase in cell death when comparing 1 and 2 stimulations, and 2 and 10 (Fig. 4F and G). Of note, the inflexion point remained unchanged (Fig. 4H). Thus, these results suggest that the number of cells undergoing pyroptosis increases with the amount of light stimulation, whereas the kinetics of the reaction remain the same.

Controlled opto-ASC activation reveals different effectiveness of three CASP1 inhibitors Next, we wondered whether the opto-ASC system stably expressed in a cell type of interest could be used to compare the efficacy of pharmacological modulators of inflammasome responses in a medium throughput approach. We applied a fixed pattern of stimulation in the absence or presence of Z-VAD-fmk, YVAD-fmk, or VX-765. Monitoring of cell death induced by opto-ASC

activation highlighted different inhibition efficacies of these three CASP1 inhibitor molecules. VX-765 appeared to be the most effective, whereas YVAD-fmk was the least potent in blocking cell death (Fig. 4 I, J, K). Opto-ASC is thus an efficient controllable tool for drug screening.

Volume measurement shows that pyroptotic swelling is a two-step mechanism

Assessing accurate volume dynamics during pyroptosis can bring new insights into the biophysical mechanisms involved in the swelling process and PMR, but such measurements remain challenging. One such limitation is due to the fact that many NLRP3 activators act at the PM by opening channels (for example, ATP through the binding to P2X7R) or by permeating the PM (for example, the nigericin pore-forming toxin) to trigger inflammasome activation (*26*). Thus, we reasoned that our optogenetic approach is perfectly suited to precisely measure the temporal relationship between ASC activation, pore opening, cell swelling and PMR during pyroptosis by combining it with a fluorescence exclusion microscopy method (FXm) (Fig. 5A) (*27*). Briefly, cells were grown in a microfluidic chamber of defined height in the presence of cell non-permeant fluorophore-coupled dextran molecules of given sizes (Fig. 5A). Images were acquired in epifluorescence at low magnification using low numerical aperture objectives. From these images, the cell volume was computed based on the exclusion of the fluorescent dextran (*27*). To follow cell swelling, pore formation and PMR concomitantly, we chose to use two different sizes of dextran (10 kDa and 500 kDa) coupled to Alexa-Fluor 647 and TRITC, respectively. Indeed, the 10 kDa Small Dextran (SD) has a small hydrodynamic radius ($R./ < 2nm$) and can thus cross the GSDMD pores (*28*), whereas the 500 kDa Large Dextran (LD) has a hydrodynamic radius ($R0/ = 15.9nm$) larger than the GSDMD pores ($R1234 = 10.75nm$) that will only enter cells upon PMR (*29*) (Fig. 5A). Pyroptosis was induced using either light activation of opto-ASC or ATP as a standard NLRP3 inflammasome activator. Nigericin, which is only soluble in organic solvents like ethanol, was inefficient in these microfluidic chambers most probably due to polydimethylsiloxane (PDMS) hydrophobicity preventing the use of such activators (*30*). Two representative examples of FXm data obtained upon pyroptosis induction from an individual cell are shown in Fig. 5B (opto- ASC) and 5C (ATP), and the associated mean volume trajectories are shown in fig. S5A and C. Upon light activation of opto-ASC, cells started to swell until they reached maximum volumes. Then, the measured volume started to decrease as cells became permeable to dextrans, indicating a loss of PM integrity (Fig. 5B and fig. S5A). A similar pattern was observed for ATP-induced pyroptosis although the volumes, temporal dynamics and swelling rates were different (Fig. 5C and fig.

S5C). No change in volume was observed without light illumination (fig. S5C). In both conditions, two successive phases were observed. The first phase displayed similar patterns of cell swelling for both small and large dextrans until the volume stabilized. During the second phase, the small dextran entered cells as evidenced by a drop in volume, whereas the large dextran did not enter cells and indicated that cells kept swelling until they reached a maximum size before PMR occurred (Fig. 5B and C and fig. S5A and C). This result indicates that the small dextran entered the cell whereas the process of swelling did not reach its maximum, suggesting the entry of the small dextran upon GSDMD pore formation and prior to PMR (large dextran entry) (Fig. 5D and E).

We then compared the global ATP response to opto-ASC activation in terms of cell swelling and PMR (Fig. 5D-G, and fig. S5D and E). The increase in relative cell volume observed with the small dextran was significantly lower upon opto-ASC activation (36 +/- 3%) than upon ATP activation (122 +/- 7%) (Fig. 5D), but the volume at lysis was similar for both conditions ($\Delta V/V$ = 135 +/- 10 for opto-ASC activation and 145 +/- 10 for ATP) (Fig. 5E). Larger delays 5 in both phases showed that the whole process was slower upon ATP activation, most likely due to the necessary time for downstream signaling pathways to activate the inflammasome (Fig. 5F and G). However, the rate of volume increase was higher upon opto-ASC activation for the two swelling phases (Phase 1: 400 +/- 20 µm3/min versus 236 +/- 15 µm3/min for ATP; phase 2: 380+/-20 µm3/min versus 280 +/- 20 µm3/min for ATP) (fig. S5D and E). Overall, these results demonstrate that the combination of FXm and opto-ASC is well-suited to study PM swelling and rupture and reveals that inflammasome activation induces a two-step cell swelling.

Inflammasome-induced PMR is an active process

Our results showed that during pyroptosis and for both light and ATP activation, cells double in size before PMR. PMR downstream of inflammasome activation has often been suggested to originate from PM mechanical stress following an osmotic imbalance due to pore formation (*31*). We therefore induced an increase in volume similar or larger than the one occurring during pyroptosis by submitting iBMDMs to osmotic shocks. To that effect, three hypo-osmotic stresses ranging from 90 to 235 mOsm were applied to cells to induce passive swelling and volume adaptation (Fig. 5H and I). The data obtained showed that the 3 stresses induced moderate to large increases in cell volumes, but not PMR, as cells returned to their original size after swelling through regulatory mechanisms (*32*). The maximum volumes reached were

in accordance with theoretical predictions from the Ponder – Van't Hoff model and provided an estimation of the osmotically inactive volume (Vi) for iBMDMs cells of 36% in agreement with previous works (fig. S5F) (*33*, *34*). The 90 mOsm stress nearly tripled the size of cells without inducing PMR, demonstrating that iBMDM have sufficient quickly available plasma membrane to sustain large deformations without undergoing PMR (Fig. 5H, I). Since inflammasome activation using either opto-ASC or ATP induced PMR when cells reached twice their volume, we concluded that the PMR associated with pyroptosis is not a passive process due to osmotic shock but is most likely a biologically controlled process that promotes plasma membrane weakening (Fig. 5J).

Discussion

Inflammasome formation results in three main biological outcomes: the formation of specks, the maturation and secretion of inflammatory cytokines, and pyroptosis. Here, we generated a new specific photoactivable inflammasome, opto-ASC, based on optogenetic methods using the photosensitive element CRY2 which was designed to activate the inflammasome in a PAMP- and DAMP-independent manner. We provide proof-of-concept that an optogenetic approach is a useful tool suitable to control and dissect inflammasome signaling based on its fast activation. This approach is therefore more powerful than other reverse engineering systems based on chemical dimerization that are slower, more difficult to monitor and based on drug treatment (*35*). We demonstrated that we were able to uncouple cytokine production from pyroptosis and to reconstitute inflammasome-deficient cells with minimal components. This tool is thus relevant to many cell types of interest. In addition, the opto-ASC system could also be useful to explore encoded signals involved in inflammasome activation using genetic or chemical screens. Similar approaches have coupled optogenetic modules to different cell death effectors (CDE) to compare, in vivo, the impact of different cell death modes on tissues, to GSDMD truncated protein to assess the regulation of GSDMD pore formation, or to CAR T cell to promote cell death, re-enforcing the usefulness of these approaches to dissect specific signaling pathways (*36*–*38*). Moreover, in zebrafish, the introduction of an opto-ASC construct revealed that cells undergoing pyroptosis are extruded from the tissue, an observation that is consistent with the ones made with opto-CASP1 (*36*, *39*). However, no optogenetic approach has been designed to control inflammasome assembly in mammalian cells. Moreover, to study the output of inflammasome activation, using an opto-ASC rather than an opto-CDE is closer

to physiological conditions since we manipulate the assembly of the inflammasome platform and not only the effectors. It therefore provides a complementary tool to investigate the mechanism of inflammasome assembly and screen inhibitory drugs targeting upstream effector mechanisms.

An optogenetic approach does not only offer fast activation but also reversible activation. Indeed, 4-6 min post-illumination, the CRY2 complex dissociates, and this property is frequently used to study the dynamics of complex dissociation (*40*). For instance, P. Broz's team, who coupled optogenetic to CASP1, was able to induce sub-lethal pyroptosis with transient light activation (*36*). Hence, 4-6 min after stimulation, ASC specks could be predicted to dissociate. However, here, in conditions in which pyroptosis was prevented by adjunction of a CASP1 inhibitor or by working in inflammasome-deficient cells, we observed that ASC specks did not dissociate after 10 min post-stimulation, supporting the notion that ASC behaves like a prion protein in vivo due to intrinsic oligomerization properties of its PYD and CARD and that inflammasome assembly follows an all-or-nothing pattern (*21*, *22*). Thus, opto-ASC could be useful to study speck assembly, binding properties of specific ASC mutants or to discover novel functions unrelated to the inflammasome.

Our results suggest that ATP by itself also affects cell volume upstream of inflammasome activation which is in accordance with the fact that ATP binding to P2X7R opens a cation-selective channel(*41*). Our results also highlight that upon GSDMD pore formation, cells kept swelling to double in size before PMR occurred. Hence, our opto-ASC construct enabled us to uncouple the signaling events upstream of inflammasome activation (for example P2X7R opening) from the downstream effects of CASP1 activation to measure events exclusively related to inflammasome activation, that is, cell swelling, GSDMD pore formation and PMR. Here, we report precision measurements of cell volume increase during pyroptosis. A previous approach based on PM labeling estimated the increase in cell volume of about 50% upon PAMP stimulation of the inflammasome (*17*). Here, we unraveled that the cell swelling caused by the sole CASP1 activation is about 100% of the initial cell volume. Following classical osmotic stress, the cell volume increased by about 200% without undergoing PMR. Thus, during pyroptosis, cell swelling and PMR are tightly coupled mechanisms. Unlike the model proposed by Davis *et al.*, suggesting that in vitro pyroptotic cells remain swollen, and that PMR occurs through mechanical stress like shear stress, we demonstrated using a large dextran that

inflammasome activation induces PMR after the swelling phase (*31*). Our results are consistent with findings that PMR is an active mechanism driven by NINJ1 activation (*10*).

Our opto-ASC tool also revealed that during pyroptosis, cell swelling occurred in two phases, with an intermediate plateau that most likely reflects the formation of GSDMD pores (Fig. 5J). Future quantitative analyses using opto-ASC may unveil the molecular mechanisms controlling the GSDMD pore formation and the biophysics of PMR. Finally, we hope that this type of approach will offer new perspectives in the field of innate immunity to refine PRR signaling.

Materials and methods Reagents:

Z-YVAD-fmk (YVAD-fmk) and Z-VAD-fmk were purchased from Bachem and Enzo Life sciences. TO-PRO3TM Ready FlowTM Reagent and Alexa-Fluor 647-Dextran 10,000 Da was from Thermofisher and TRITC-Dextran 500,000 Da from Tdb Labs (Sweden) and Polydimethylsiloxane (PDMS) Sylgard 184 from Dow Corning. Nigericin (N7143) and ATP (A6419) were from Sigma Aldrich. Glycine was purchased from Euromedex. Ultra-pure LPS (*Escherichia coli* 0111:B4) and VX-765 were purchased from Invivogen.

Cell lines

HEK-293T (human embryonic kidney 293T cells) and Phoenix-Eco packaging cells were purchased from ATTC. HEK-293 FT were a kind gift of Dr Nègre from the ANIRA platform. Murine iBMDM (immortalized bone marrow-derived macrophages), cell lines were a kind gift from P. Broz and E. Latz (*42*, *43*). Cells were cultured with DMEM 4.5 g/L glucose (Gibco) supplemented with 10% FBS, 1% penicillin-streptomycin, 1% Glutamax and 1% sodium pyruvate (all Invitrogen). MEF were generated by O. Destaing (*44*). Cells were mycoplasma-free and routinely tested for mycoplasma.

Cloning of opto-ASC construct and stable expression in iBMDM

In this study, human ASC, CRY2 and TagRFP were cloned into a pSico R vector (Addgene 11579) digested with Nhe1/Eco R1. The CAG promoter was then cloned into this vector in order to moderate overexpression of opto-ASC and make its expression less sensitive to methylation processes occurring in numerous primary cell types. The pSico-CAGpromoter- CRY2-TagRFP backbone (sequence available in the Supplementary table) was thus obtained by amplification with PHUSION high fidelity DNA polymerase (NEB) and using Gibson assembly (NEB) following

the supplier's instruction and the indicated primers: primer asc fwd = ttagtgaaccgtcagatccgctagcATGGG GCG CGC GCG CGA C, primer asc rvs = ccatcttcatcttaa ttaaGCTCCGCTCCAGGTCCTCCACC, primer cry2 fwd = ggagcggagcttaattaaGATGAAGATGGACAAAAAGACTATAG, primer cry2 rvs = cttaat cagctcgctcatttcgaaTGCTGCTCCGATCATGATC, primer TagRFP fwd = GATCATGATCGGAGCAGCATTCGAAATGAGCGAGCTGATTAAG, primer Tag RFP rvs = agttattaggtccctcgacgaattctcaCTTGTGCCCCAGTTTGC, primer CAG fwd = agtactaggatccattaggcggccgcGAGTTCCGCGTTACATAACTTAC, primer CAG rvs = cgtcgcgcgcgcgccccatgctagTGATGAGACAGCACAATAAC

Lentivirus production, cell infection and sorting

Lentiviruses were produced by co-transfecting pC57GPBEB GagPol MLV, pSUSVSVG and each plasmid of interest using lipofectamine 2000 (Invitrogen) in HEK-293 FT cells plated in 6-well plates at 50% confluency. Medium was changed 24 h later. The viral supernatant was collected 72 h later and filtered using 0.45 µm filters. iBMDM were plated in 6-well plates at 60% confluency the day of infection. The filtered supernatant was directly used to infect cells of interest. The medium was changed 24 h after infection. After 10 days, cells were FACS sorted (Aria cell sorter 2000, or Aria III using Diva software, BD Biosciences) based on the level of expression of RFP-tagged opto-ASC using 561 nm laser.

Retroviral transduction

The plasmid encoding GFP-IRES-CASP1 was obtained from P. Broz (*3*, *45*). To produce retroviral particles, Phoenix-Eco packaging cells were co transfected with pMSC2.2-expressing vectors for CASP1 using lipofectamine 2000 reagent (life technologies). The medium was removed after 24 h and replaced with fresh complete medium. After 48 h the medium was filtered twice using 0.45µm filters. MEFs were transduced, isolated and sorted on FACS Aria III (BD Biosciences) using Diva software (BD Biosciences).

Live imaging of pyroptosis process

Cells were seeded into Lab-Tek II chamber Slide (Nunc, Roskilde, Denmark) in phenol-red free medium, 24 h before imaging. Cellular viability was assessed using TO-PRO-3 Ready FlowTM Reagent (dilution: 1/2000). Optogenetic model activation and pyroptosis process imaging was performed in controlled atmosphere 37°C, 5 % CO2, with confocal fluorescence microscope

LSM-880 Zeiss (Objective 40x NA 1.3). Cells were illuminated 3 times every 10 seconds with 488nm laser (Light dose 45 mJ/cm2). 30 min later, speck formation (RFP) and dying cells were imaged using 561 and 633 nm lasers, respectively. Image analysis was performed with Fiji software. For live-cell tomography images acquisition, cells were seeded on µ-Dish 35 mm high (ibidi) plates 24 h before imaging with Nanolive 3D Cell Explorer-Fluo.

Caspase inhibitors

To prevent pyroptosis, cells were pre-treated with either CASP1 inhibitors VX-765 (50 µM) or YVAD-fmk (50 µM) or pan caspase inhibitor Z-VAD-fmk (50 µM) 30 min before inflammasome activation.

IL-1b, **IL-18 and LDH release analysis**

24 h after plating, cells were primed or not with LPS 0.5 µg/ml for 3 h and treated or not with CASP1 inhibitor (VX-765) 50 µM for 30 min in optiMEMTM serum-free medium. Cells were illuminated or not 50 times with 0.8s flash using an incubator equipped with blue LED (1.8 mW) as initially described by the lab of Janovjak (Light dose 42 mJ/cm2) (*46*). 1 h after illumination, dosage of IL-1b, IL-18 and LDH released were quantified on cell supernatants with a mouse IL-1β/IL-1F2 DuoSet ELISA (R&D Systems), IL-18 BMS-618-3 (Invitrogen) and CytoTox 96 Non-Radioactive Cytotoxicity Assay (Promega, France), respectively. For nigericin or ATP treatment, cells were first primed with LPS 0.5 µg/ml for 3 h then treated with either ATP 5 mM 1h or nigericin 10 µM 3h. For glycine treatment, cells were pre-treated with glycine 20 mM.

Immunoblots

Cell lysates and cell supernatants were processed separately, as described by Guey *et al.*, with the following modification, cell pellets were lysed in Laemmli buffer x2 (Tris HCl 0.5 M pH 6.8; 0.5 M DTE; 0.5% SDS) and semi-dry transfer was carried using the Transblot turbo system from Biorad (*47*).

The following antibodies were used: ASC Ab AL177, CASP1 AG-20B-0042 (Casper) from Adipogen; tRFP AB233 from Evrogen; IL-1b AF-401-NA from R&Dsystems; GSDMD EPR19828 ab209845 from Abcam; NINJ1 sc-136295 Santa Cruz; actin C4 ICN-MP; tubulin CP06 from

Millipore; Rabbit Peroxidase anti-rabbit 715-035-150, Mouse Peroxidase anti- mouse 711-035-152 and Goat Peroxidase anti-goat 705-035-147 from Jackson Immunoresearch.

Gradual activation of opto-ASC cells with the Operetta CLS

Death induction followed by light illumination was monitored at 37°C, 5% CO2 using TO- PRO-3 for cell viability and a Perkin Elmer Operetta CLS High-Content Analysis System (20x water-objective) controlled by Harmony software (Perkin Elmer, Germany). Light activation was performed with 488 nm LED of Operetta microscope. Opto-ASC expressing iBMDMs were activated by 3 light stimulations of increasing LED intensity (1, 5, 10 or 15 % of LED power) or an increasing number of light stimulations with a fixed LED intensity of 10 %. For the assessment of CASP1 inhibitors activities, cells received 3 stimulations of 10% intensity. Image quantification was conducted with Columbus software (Perkin Elmer, Germany).

Power density table:

LED power (%)	fluency (mJ/cm²)	Nb of stim	fluency (mJ/cm²)
1	2,851675579	1	75,25254999
2	16,63477421	2	150,5051
5	102,1850416	3	225,75765
10	225,75765	10	752,5254999

Immunofluorescence staining

Cells were plated on sterile glass coverslips, illuminated 50 times (0.8s) using the incubator equipped with blue LED (Light dose: 42 mJ/cm2). Cells were then fixed with PBS-PFA 2% for 5 min at room temperature, permeabilized with PBS-Triton 0.5%, and blocked in PBS-FBS 3% for 30 min. Primary antibody anti-CASP1 (1:100, Casper-1) was diluted in PBS-FBS 3% and incubated over 30 min at room temperature. Cells were then incubated with Alexa-Fluor 488-conjugated anti-mouse (1:500; Life Technologies) or Alexa-Fluor 680-conjugated anti-rabbit (1:500; Life Technologies) antibodies for 30 min at room temperature in the dark and in

Hoechst (500 ng/mL in PBS) for 5 min. Slides were imaged using confocal Nikon Ti-2 microscope (Nikon) equipped with a Yokogawa CSU-W1 spinning disk (Yokogawa) and analyzed with FIJI software.

Fabrication of FXm chips

Chips were made by pouring PDMS elastomer and curing agent (1:10, Sylgard 184 from Dow Corning) on a mold and was cured for at least 2 h at 65°C. Molds were made on a silicon wafer with SU-8 photoresist using classical photolithography techniques. 3 mm inlets and outlets in the PDMS were punched and the PDMS chips were cut to fit on glass coverslips. The coverslips were bond onto 35 petri dishes with Norland Optical Adhesive 81 (Norland) for 1 minute at UV 324 nm. Chips were bonded to glass coverslips by exposure to oxygen plasma for 30 s, and dried for 5 min at 65°C immediately after bonding. These systems could then be stored for a week at +4°C and washed with PBS prior to seeding cells.

Volume measurement with FXm

Cell volumes were obtained using the fluorescence exclusion method (FXm) as detailed in (*27*, *48*). Briefly, 5x10^4 cells were plated on PDMS chip with complete medium supplemented with HEPES a day before experiments. ATP-treated cells were primed with LPS. For volume measurement, phenol red free medium was supplemented with a fluorescent dye coupled dextran molecules. Fluorescence was thus excluded by the cells and cell volumes were obtained by integrating the fluorescence intensity over the cell. Excitation and acquisition were performed at 37°C in CO2-independent medium (Life Technologies) supplemented with 1 g/L Alexa Fluor 647 dextran (10 kDa) and TRITC dextran (500 kDa) using an epifluorescence microscope (Leica DMi8) with a 10x objective (NA. 0.3, LEICA). Light activation was performed with 488 nm LED (25% of a PE300 LED from CoolLED) during 10 s (Light dose 3720 mJ/cm2). Image analysis was performed using a homemade MatLab program adapted from (*27*, *48*). Briefly, for every time frame, the fluorescence background is subtracted for each cell and the linear relation between fluorescence and height calibrated for each field on view.

32

For multiple dyes, cell segmentation is systematically performed on the images of the largest dye since it is the latest to enter the cells. The fluorescence drop is integrated over the aera of

each cell obtained from the segmentation and computed in volume using the relation between fluorescence and height obtained previously.

For osmotic shocks experiments, hypotonic solutions were generated by addition of dH20 to imaging medium. Then, Alexa Fluor 647 dextran (10 kDa) resuspended in PBS was added at a final concentration of 1 g/L. Each experiment is the result of the analysis of 2 independent chips. Analyses were performed using homemade Matlab scripts (MathWorks).

Statistical analysis

All data were analyzed with GraphPad Prism 9.0 (San Diego, CA, USA). Data are expressed as mean ± S.D. The statistical significance between experimental conditions was determined by contingency table using the Fisher test or two-tailed Mann-Whitney test. **** P<0.0001, *** P<0.001, ** P<0.01, * P<0.05. ns stands for not significant.

References

1. K. Schroder, J. Tschopp, The inflammasomes. *Cell* **140**, 821–32 (2010).
2. T. Fernandes-Alnemri, J. Wu, J.-W. Yu, P. Datta, B. Miller, W. Jankowski, S. Rosenberg, J. Zhang, E. S. Alnemri, The pyroptosome: a supramolecular assembly of ASC dimers mediating inflammatory cell death via caspase-1 activation. *Cell Death Differ* **14**, 1590–604 (2007).
3. B. Guey, M. Bodnar, S. N. S. N. S. N. Manié, A. Tardivel, V. Petrilli, Caspase-1 autoproteolysis is differentially required for NLRP1b and NLRP3 inflammasome function. *Proc Natl Acad Sci U S A* **111**, 17254–9 (2014).
4. Y. Qu, S. Misaghi, A. Izrael-Tomasevic, K. Newton, L. L. Gilmour, M. Lamkanfi, S. Louie, N. Kayagaki, J. Liu, L. Kömüves, J. E. Cupp, D. Arnott, D. Monack, V. M. Dixit, Phosphorylation of NLRC4 is critical for inflammasome activation. *Nature* **490**, 539–542 (2012).
5. S. L. Fink, B. T. Cookson, Caspase-1-dependent pore formation during pyroptosis leads to osmotic lysis of infected host macrophages. *Cell Microbiol* **8**, 1812–25 (2006).
6. X. Liu, Z. Zhang, J. Ruan, Y. Pan, V. G. Magupalli, H. Wu, J. Lieberman, Inflammasome-activated gasdermin D causes pyroptosis by forming membrane pores. *Nature* **535**, 153–158 (2016).

33

7. J. Shi, Y. Zhao, K. Wang, X. Shi, Y. Wang, H. Huang, Y. Zhuang, T. Cai, F. Wang, F. Shao, Cleavage of GSDMD by inflammatory caspases determines pyroptotic cell death. *Nature* **526**, 660–665 (2015).
8. L. Sborgi, S. Rühl, E. Mulvihill, J. Pipercevic, R. Heilig, H. Stahlberg, C. J. Farady, D. J. Müller, P. Broz, S. Hiller, GSDMD membrane pore formation constitutes the mechanism of pyroptotic cell death. *EMBO J* **35**, 1766–1778 (2016).
9. J. Ding, K. Wang, W. Liu, Y. She, Q. Sun, J. Shi, H. Sun, D. Wang, F. Shao, Pore- forming activity and structural autoinhibition of the gasdermin family. *Nature* **535**, 111–116 (2016).
10. N. Kayagaki, O. S. Kornfeld, B. L. Lee, I. B. Stowe, K. O'Rourke, Q. Li, W. Sandoval, D. Yan, J. Kang, M. Xu, J. Zhang, W. P. Lee, B. S. McKenzie, G. Ulas, J. Payandeh, M. Roose-Girma, Z. Modrusan, R. Reja, M. Sagolla, J. D. Webster, V. Cho, T. D. Andrews, L. X. Morris, L. A. Miosge, C. C. Goodnow, E. M. Bertram, V. M. Dixit, NINJ1 mediates plasma membrane rupture during lytic cell death. *Nature* **591**, 131– 136 (2021).
11. L. Broderick, D. De Nardo, B. S. Franklin, H. M. Hoffman, E. Latz, The Inflammasomes and Autoinflammatory Syndromes. *Annual Review of Pathology: Mechanisms of Disease* **10**, 395–424 (2015).
12. E. Aganna, F. Martinon, P. N. Hawkins, J. B. Ross, D. C. Swan, D. R. Booth, H. J. Lachmann, A. Bybee, R. Gaudet, P. Woo, C. Feighery, F. E. Cotter, M. Thome, G. a Hitman, J. Tschopp, M. F. McDermott, Association of mutations in the NALP3/CIAS1/PYPAF1 gene with a broad phenotype including recurrent fever, cold sensitivity, sensorineural deafness, and AA amyloidosis. *Arthritis Rheum* **46**, 2445–52 (2002).
13. F. Martinon, V. Petrilli, A. Mayor, A. Tardivel, J. Tschopp, V. Pétrilli, A. Mayor, A. Tardivel, J. Tschopp, V. Petrilli, A. Mayor, A. Tardivel, J. Tschopp, V. Pétrilli, Gout- associated uric acid crystals activate the NALP3 inflammasome. *Nature* **440**, 237–241 (2006).
14. P. Duewell, H. Kono, K. J. Rayner, C. M. Sirois, G. Vladimer, F. G. Bauernfeind, G. S. Abela, L. Franchi, G. Nuñez, M. Schnurr, T. Espevik, E. Lien, K. a Fitzgerald, K. L. Rock, K. J. Moore, S. D. Wright, V. Hornung, E. Latz, NLRP3 inflammasomes are required for atherogenesis and activated by cholesterol crystals. *Nature* **464**, 1357–61 (2010).
15. B. Vandanmagsar, Y.-H. Youm, A. Ravussin, J. E. Galgani, K. Stadler, R. L. Mynatt, E. Ravussin, J. M. Stephens, V. D. Dixit, The NLRP3 inflammasome instigates obesity-induced inflammation and insulin resistance. *Nat Med* **17**, 179–88 (2011).

16. M. Groslambert, B. Py, Spotlight on the NLRP3 inflammasome pathway. *J Inflamm Res* **Volume 11**, 359–374 (2018).
17. N. M. de Vasconcelos, N. Van Opdenbosch, H. Van Gorp, E. Parthoens, M. Lamkanfi, Single-cell analysis of pyroptosis dynamics reveals conserved GSDMD-mediated subcellular events that precede plasma membrane rupture. *Cell Death Differ* **26**, 146–161 (2019).
18. L. J. Bugaj, A. T. Choksi, C. K. Mesuda, R. S. Kane, D. V Schaffer, Optogenetic protein clustering and signaling activation in mammalian cells. *Nat Methods* **10**, 249– 252 (2013).
19. R. M. Hughes, D. J. Freeman, K. N. Lamb, R. M. Pollet, W. J. Smith, D. S. Lawrence, Optogenetic Apoptosis: Light-Triggered Cell Death. *Angewandte Chemie International Edition* **54**, 12064–12068 (2015).

34

20. M. J. Kennedy, R. M. Hughes, L. a Peteya, J. W. Schwartz, M. D. Ehlers, C. L. Tucker, Rapid blue-light-mediated induction of protein interactions in living cells. *Nat Methods* **7**, 973–975 (2010).
21. A. Lu, V. G. Magupalli, J. Ruan, Q. Yin, M. K. Atianand, M. R. Vos, G. F. Schröder, K. A. Fitzgerald, H. Wu, E. H. Egelman, Unified polymerization mechanism for the assembly of ASC-dependent inflammasomes. *Cell* **156**, 1193–1206 (2014).
22. X. Cai, J. Chen, H. Xu, S. Liu, Q.-X. Jiang, R. Halfmann, Z. J. Chen, Prion-like Polymerization Underlies Signal Transduction in Antiviral Immune Defense and Inflammasome Activation. *Cell* **156**, 1207–1222 (2014).
23. S. Mariathasan, D. S. Weiss, K. Newton, J. McBride, K. O'Rourke, M. Roose-Girma, W. P. Lee, Y. Weinrauch, D. M. Monack, V. M. Dixit, Cryopyrin activates the inflammasome in response to toxins and ATP. *Nature* **440**, 228–232 (2006).
24. Y. Cotte, F. Toy, P. Jourdain, N. Pavillon, D. Boss, P. Magistretti, P. Marquet, C. Depeursinge, Marker-free phase nanoscopy. *Nat Photonics* **7**, 113–117 (2013).
25. J. P. Borges, R. S. R. Sætra, A. Volchuk, M. Bugge, P. Devant, B. Sporsheim, B. R. Kilburn, C. L. Evavold, J. C. Kagan, N. M. Goldenberg, T. H. Flo, B. E. Steinberg, Glycine inhibits NINJ1 membrane clustering to suppress plasma membrane rupture in cell death. *Elife* **11**, e78609 (2022).

26. V. Pétrilli, C. Dostert, D. a D. A. Muruve, J. Tschopp, V. Petrilli, C. Dostert, D. a D. A. Muruve, J. Tschopp, The inflammasome: a danger sensing complex triggering innate immunity. *Curr Opin Immunol* **19**, 615–22 (2007).
27. E. Zlotek-Zlotkiewicz, S. Monnier, G. Cappello, M. Le Berre, M. Piel, Optical volume and mass measurements show that mammalian cells swell during mitosis. *Journal of Cell Biology* **211**, 765–774 (2015).
28. J. K. Armstrong, R. B. Wenby, H. J. Meiselman, T. C. Fisher, The hydrodynamic radii of macromolecules and their effect on red blood cell aggregation. *Biophys J* **87**, 4259–4270 (2004).
29. S. Xia, Z. Zhang, V. G. Magupalli, J. L. Pablo, Y. Dong, S. M. Vora, L. Wang, T.-M. Fu, M. P. Jacobson, A. Greka, J. Lieberman, J. Ruan, H. Wu, Gasdermin D pore structure reveals preferential release of mature interleukin-1. *Nature* **593**, 607–611 (2021).
30. K. J. Regehr, M. Domenech, J. T. Koepsel, K. C. Carver, S. J. Ellison-Zelski, W. L. Murphy, L. A. Schuler, E. T. Alarid, D. J. Beebe, Biological implications of polydimethylsiloxane-based microfluidic cell culture. *Lab Chip* **9**, 2132–9 (2009).
31. M. A. Davis, M. R. Fairgrieve, A. Den Hartigh, O. Yakovenko, B. Duvvuri, C. Lood, W. E. Thomas, S. L. Fink, M. Gale, Calpain drives pyroptotic vimentin cleavage, intermediate filament loss, and cell rupture that mediates immunostimulation. *Proc Natl Acad Sci U S A* **116**, 5061–5070 (2019).
32. E. K. Hoffmann, I. H. Lambert, S. F. Pedersen, Physiology of cell volume regulation in vertebrates. *Physiol Rev* **89**, 193–277 (2009).
33. L. Venkova, A. S. Vishen, S. Lembo, N. Srivastava, B. Duchamp, A. Ruppel, A. Williart, S. Vassilopoulos, A. Deslys, J. M. Garcia Arcos, A. Diz-Muñoz, M. Balland, J. F. Joanny, D. Cuvelier, P. Sens, M. Piel, A mechano-osmotic feedback couples cell volume to the rate of cell deformation. *Elife* **11** (2022).
34. C. Roffay, G. Molinard, K. Kim, M. Urbanska, V. Andrade, V. Barbarasa, P. Nowak, V. Mercier, J. García-Calvo, S. Matile, R. Loewith, A. Echard, J. Guck, M. Lenz, A. Roux, Passive coupling of membrane tension and cell volume during active response of cells to osmosis. *Proc Natl Acad Sci U S A* **118** (2021).
35. D. W. Chang, X. Yang, Activation of procaspases by FK506 binding protein-mediated oligomerization. *Sci STKE* **2003**, PL1 (2003).

35

36. K. Shkarina, E. Hasel de Carvalho, J. C. Santos, S. Ramos, M. Leptin, P. Broz, Optogenetic activators of apoptosis, necroptosis, and pyroptosis. *Journal of Cell Biology* **221**, e202109038 (2022).
37. L. He, Z. Huang, K. Huang, R. Chen, N. T. Nguyen, R. Wang, X. Cai, Z. Huang, S. Siwko, J. R. Walker, G. Han, Y. Zhou, J. Jing, Optogenetic Control of Non-Apoptotic Cell Death. *Advanced Science* **8**, 2100424 (2021).
38. L. He, P. Tan, L. Zhu, K. Huang, N. T. Nguyen, R. Wang, L. Guo, L. Li, Y. Yang, Z. Huang, Y. Huang, G. Han, J. Wang, Y. Zhou, Circularly permuted LOV2 as a modular photoswitch for optogenetic engineering. *Nat Chem Biol* **17**, 915–923 (2021).
39. E. Hasel de Carvalho, S. S. Dharmadhikari, K. Shkarina, J. R. Xiong, B. Reversade, P. Broz, M. Leptin, The Opto-inflammasome in zebrafish as a tool to study cell and tissue responses to speck formation and cell death. *Elife* **12** (2023).
40. Y. Shin, B. J, P. N, H. MP, T. JE, B. CP, Spatiotemporal Control of Intracellular Phase TransitionsUsing Light-Activated optoDroplets. *Cell* **2017 Jan 1**, 159-171.e14. (2017).
41. F. Di Virgilio, Liaisons dangereuses: P2X(7) and the inflammasome. *Trends Pharmacol Sci* **28**, 465–72 (2007).
42. R. Heilig, M. Dilucca, D. Boucher, K. W. Chen, D. Hancz, B. Demarco, K. Shkarina, P. Broz, Caspase-1 cleaves Bid to release mitochondrial SMAC and drive secondary necrosis in the absence of GSDMD. *Life Sci Alliance* **3**, e202000735 (2020).
43. V. Hornung, F. Bauernfeind, A. Halle, E. O. Samstad, H. Kono, K. L. Rock, K. a Fitzgerald, E. Latz, Silica crystals and aluminum salts activate the NALP3 inflammasome through phagosomal destabilization. *Nat Immunol* **9**, 847–56 (2008).
44. O. Destaing, E. Planus, D. Bouvard, C. Oddou, C. Badowski, V. Bossy, A. Raducanu, B. Fourcade, C. Albiges-Rizo, M. R. Block, β1A Integrin Is a Master Regulator of Invadosome Organization and Function. *Mol Biol Cell* **21**, 4108–4119 (2010).
45. P. Broz, J. von Moltke, J. W. Jones, R. E. Vance, D. M. Monack, Differential requirement for Caspase-1 autoproteolysis in pathogen-induced cell death and cytokine processing. *Cell Host Microbe* **8**, 471–83 (2010).
46. M. Grusch, K. Schelch, R. Riedler, E. Reichhart, C. Differ, W. Berger, Á. Inglés- Prieto, H. Janovjak, Spatio-temporally precise activation of engineered receptor tyrosine kinases by light. *EMBO J* **33**, 1713–1726 (2014).

47. B. Guey, V. Petrilli, “Assessing caspase-1 activation” in *Methods in Molecular Biology* (2016)vol. 1417, pp. 197–206.
48. C. Cadart, L. Venkova, P. Recho, M. C. Lagomarsino, M. Piel, The physics of cell-size regulation across timescales. *Nat Phys*, doi: 10.1038/s41567-019-0629-y (2019).

Acknowledgements:

We thank Dr. P. Recho (LIPhy) for the funding of EB and scientific discussions. We thank Pr P Broz (University of Lausanne) and Pr E Latz (Deutsches Rheuma Forschungszentrum Berlin) for sharing iBMDM cells, B. Manship (CRCL) for English editing of the manuscript and A. Tissier (CRCL) for critical reading of the manuscript.

Funding:

36

Ligue Nationale contre le cancer comité de l’Ain (VP), La Ligue Nationale Contre le Cancer (GI), LLNC as “Equipe labellisée Ligue 2014” (EL2014.LNCC) (OD), Fondation de France (GI), fondation FINOVI (BP, VP), Institut Convergence PLAsCAN, ANR-17-CONV-0002 (VP, SM), Fondation pour la Recherche Médicale as « équipe labellisée » DEQ20170336744 (VP) and DEQ20170336702 (OD), LabEx DEVweCAN (University of Lyon, GI), CLARA cancéropole (VP), Agence Nationale de la Recherche (ANR) Young Researchers Project ANR- 18-CE13-0005-01 (GI), ANR-13-JSV2-0003-01(OD), ANR-20-CE15-0033 (ALH) and PRC ANR-19-CE13-0030 (EB), ANR-22-CE15-0032-01 (BP, VP), ERC-2013-CoG_616986 (BP), Marie Sklodowska-Curie fellowship n°751216 (ALH), the fondation Line Pomaret Delalande PLP202110014593 (LB).

Author Contributions:

V.P. and O.D. conceptualized the project. J.N, S.M., E.B. C.V. and A.-L.H developed the methodology used. J.N, S.M., E.B., A.-L.H, C.O., LB., H.B.L., G.I., B.P., O.D., and V.P. conducted investigations. V.P., O.D., B.P. and S.M. acquired funding. S.M., E.B., O.D. and V.P. wrote the manuscript.

Competing Interests: The authors declare no conflict of interest.

Data and materials availability: All data needed to evaluate the conclusions in the paper are present in the paper or the Supplementary Materials. Until its deposition and accessibility in addgene, the plasmids require a material transfer agreement from DR11-Alpes CNRS, France.

Figure 1: Schematic representation of NLRP3 inflammasome and opto-ASC activations.

37

Physiological model: (1) TLR4 activation by LPS induces the priming signal which is required for the production of proIL-1ß and NLRP3 proteins. The priming signal also modulates NLRP3 post-translational modifications (PTMs). ProIL-18 is present basally in cells. (2) ATP or nigericin is sensed by NLRP3, induces PTMs and (3) promotes NLRP3 oligomerization, which recruits ASC and CASP1 to form the multiprotein complex named inflammasome. (4) This results in the formation of a large oligomer containing ASC and CASP1 named speck, and in the activation of CASP1. (5) Active CASP1 cleaves its substrates the proIL-1ß, proIL-18 into mature cytokines and gasdermin-D (GSDMD) releasing the N-terminal fragment that integrates the plasma membrane to form pores. (6) GSDMD pores allow the release of mature cytokines, (7) ion flux and cell swelling, and (8) plasma membrane rupture leading to LDH release through the activation of NINJ1 by an unknown mechanism.

Optogenetic model: To bypass signals 1 and 2, the core inflammasome protein ASC was coupled to the blue light sensitive photolyase domain of Cryptochrome 2 (CRY2), and an RFP tag was added for visualization. Blue light stimulation promotes CRY2 dimerization, leading to ASC oligomerization followed by the recruitment and activation of CASP1, resulting in cytokine maturation and pyroptosis.

Figure 2: Light activation of opto-ASC induces CASP1 activation, IL-1b **maturation and pyroptosis.**

(A) Representative images of iBMDM stably expressing opto or opto-ASC activated or not (dark) with blue light stimulation (488 nm). Speck formation (RFP+) and cell death (TO-PRO-3+) were monitored post-stimulation using confocal microscopy in the presence or absence of the CASP1 inhibitor, VX-765. Positive TO-PRO-3 nuclei were quantified and presented on a graph. A Fisher test was used for statistical analysis. Scale bar = 10 µm. n ≥ 179 cells, from N=6 independent experiments. (B, C) Opto-ASC-expressing iBMDM were pre-incubated or

38

not with LPS then subjected to blue light and LDH release (B) n=6 from N=2 independent experiments, or IL-1b secretion (C) were assessed in supernatants, n=4 from N=2 independent experiments. A Mann-Whitney test was used for statistical analysis, mean ± S.D. **** P<0.0001, *** P<0.001. (D) Representative immunoblot of CASP1 maturation, IL-1b and GSDMD cleavage upon increasing numbers of blue light activation of opto-ASC-expressing or parental iBMDM pre-treated with LPS in the presence or absence of VX-765. Tubulin was used

as a loading control. 0 stimulation is dark condition. One representative experiment from N= 3 independent experiments.

Figure 3: The activity of opto-ASC is GSDMD- and inflammasome-dependent. (A) WT or *Gsdmd*-deficient iBMDM stably expressing opto-ASC were stimulated using a blue light confocal microscope. Speck formation was monitored through RFP+ staining and cell death through nuclear TO-PRO-3+ staining after stimulation. n≥ 48, performed over N=2 independent experiments (B) MEFs stably transduced with opto-ASC or opto-ASC and GFP-IRES-CASP1 constructs were stimulated as described in A. Speck formation was monitored through RFP+ signal and cell death through nuclear TO-PRO-3+ staining, VX-765 was added whenever indicated. n ≥ 67 performed over N= 3 independent experiments. White arrows indicate ASC-RFP specks and black arrows indicate plasma membrane (PM) swelling. Scale bar = 10 µm. Positive TO-PRO-3 nuclei were quantified and presented on a graph. A Fisher test was used for statistical analysis. *** P<0.001.

Figure 4: Controlled opto-ASC activation reveals efficacies of different CASP1 inhibitors. Opto-ASC iBMDM were stimulated using the Operetta CLS microscope and nuclear TO-PRO-3+ staining was monitored as an indicator of cell death over time (A, C, F and I). (A) Representative time-lapse images showing TO-PRO-3+ and RFP+ cells. (B) A sigmoid function

was used to fit the proportion of TO-PRO-3+ cells to extrapolate the maximum of dead cells at the end of the experiment (Dead cells max, Adead) and the time corresponding to 50% of those dead cells (Point of inflection, t1/2). (C) Different laser intensities were applied (1%, 5%, 10% or 15%) to cells with a fixed number of 3 stimulations n ≥ 300, performed over 2 independent experiments. Each experiment includes 3 biological replicates or (F) an increasing number of stimulations was applied to cells with a fixed laser intensity of 10%. n ≥ 2000 performed over 2 independent experiments including 3 biological replicate each. Using the sigmoid function described in B and applied to the data in C and F we extrapolated the percentage of cell death (in D and G) and the inflection point (time corresponding to 50% of cell response, in E and H). (I) The cells were stimulated using a fixed pattern of 3 stimulations, laser set at 10% in the presence or absence of different caspase inhibitors. (J) Percentage of cell death and (K) inflection points were extrapolated using sigmoid curves on data presented in I. n ≥ 800 performed over 2 independent experiments with 2 biological replicates each.

Mann-Whitney tests were used for statistical analysis, mean ± S.D. **** P<0.0001, *** P<0.001, **P <0.01, * P<0.05, ns: not significant.

Figure 5: Volume measurements by FXm show that GSDMD pore formation and PM lysis are distinct events.

(A) Schematic diagrams of the fluorescence exclusion method (FXm) with dye-coupled small (blue) and large (red) dextrans, and of their entry into cells. (B) Representative volume measurements of light-induced activation of opto-ASC iBMDM cells with a large dextran (LD, red curve) (TRITC – Dextran 500 kDa) and a small dextran (SD, blue curve) (Alexa647 – Dextran 10 kDa), with the corresponding time-lapse images obtained on a single cell by FXm . (C) Representative volume measurement of ATP-induced activation of parental iBMDM cells with large dextrans (LD, orange curve) (TRITC - dextran 500 kDa) and small dextran (SD, blue

40

curve) (Alexa647 - dextran 10 kDa) with the corresponding time-lapse images obtained on a single cell by FXm. Scale bars = 20 µm. (D) Mean increase in intermediate volume normalized against the initial cell volume, obtained with the SD for opto-ASC and ATP-stimulated cells. (E) Mean increase in maximum volume normalized against the initial cell volume, obtained with the LD for opto-ASC and ATP stimulated cells. (F) Delay between the onset of increase in cell volume and SD entry for opto-ASC or ATP-stimulated cells. (G) Delay between onset of increase in cell volume and LD entry. For D to G: n= 59 cells, for opto-ASC conditions, performed over 3 independent experiments including 2 independent chips each, and n=50 cells, for ATP conditions. performed over 2 independent experiments including 2 independent chips each, (H) Top: schematic diagram illustrating the increase in cell volume and adaptation measured according to the osmotic stress applied 90 (black), 138 (grey) or 235 (light grey) mOSm. Lower: Increase in iBMDM cell volume after hypo-osmotic shock. n= 39 cells for 90 mOsm, n=31 cells for 138 mOsm and n=28 cells for 235 mOsm, performed over 2 independent experiments including 2 independent chips each. (I) Relative maximum increase in cell volume before regulatory volume response occurred, extracted from data in (H). Mann-Whitney test: ** P<0.005, **** P<0.0001, mean ± S.D. (J) Illustration of the observations described in this study. The SD enters cells when GSDMD pores are formed while cells are still swelling, as observed with the LD. PMR then occurs resulting in cell lysis and entry of LD.

41

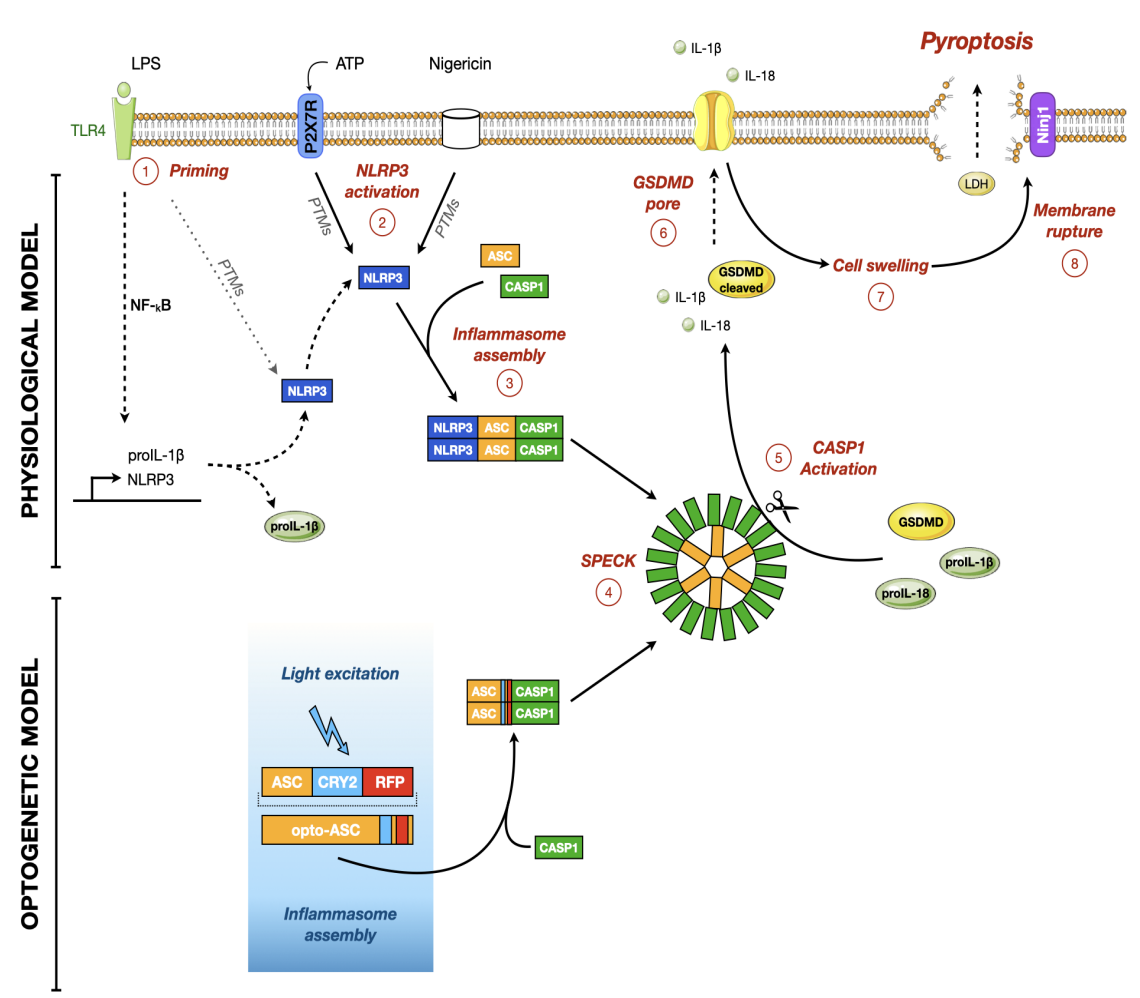

Nadjar et al. Figure 1

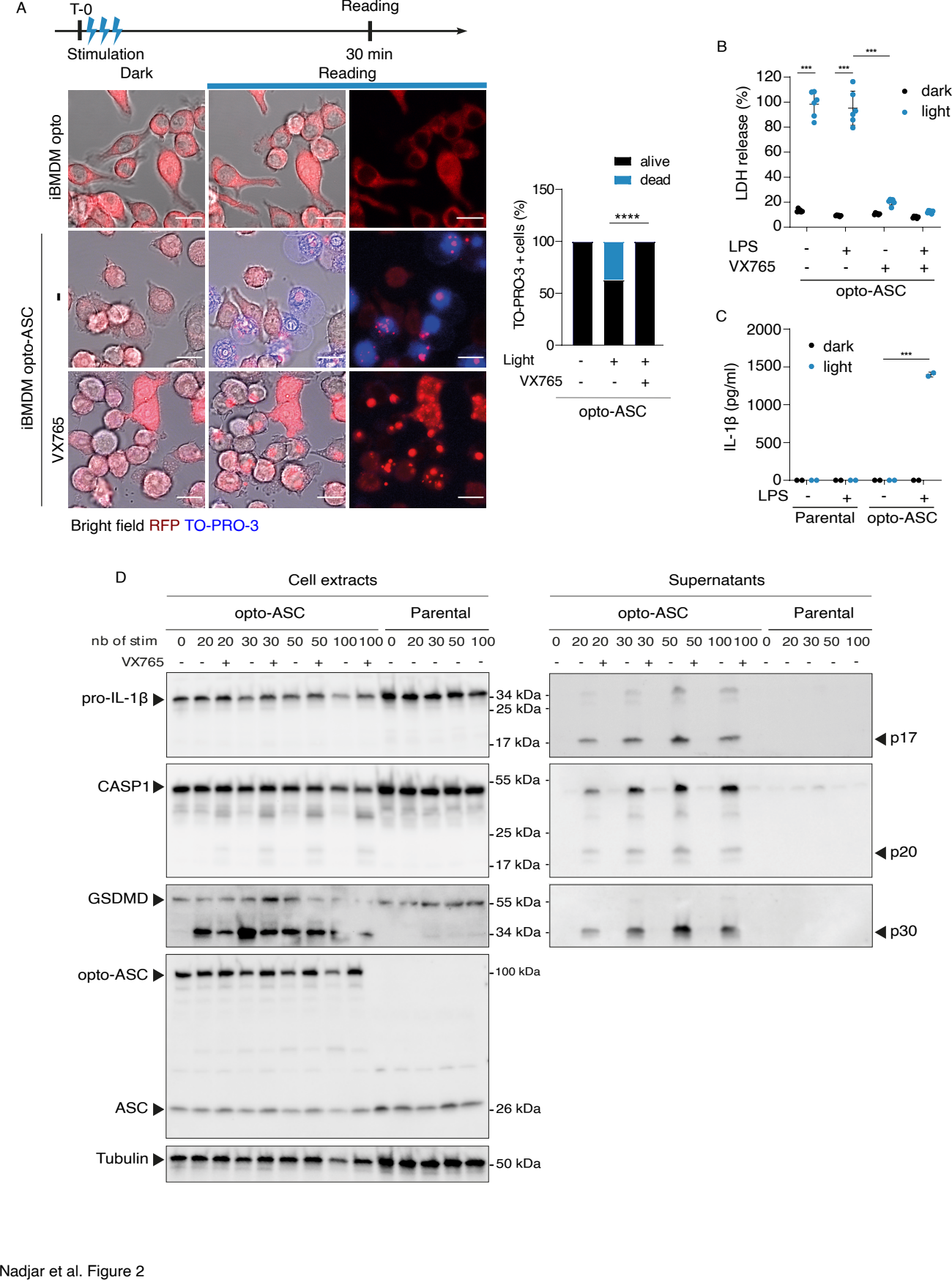

Nadjar et al. Figure 2

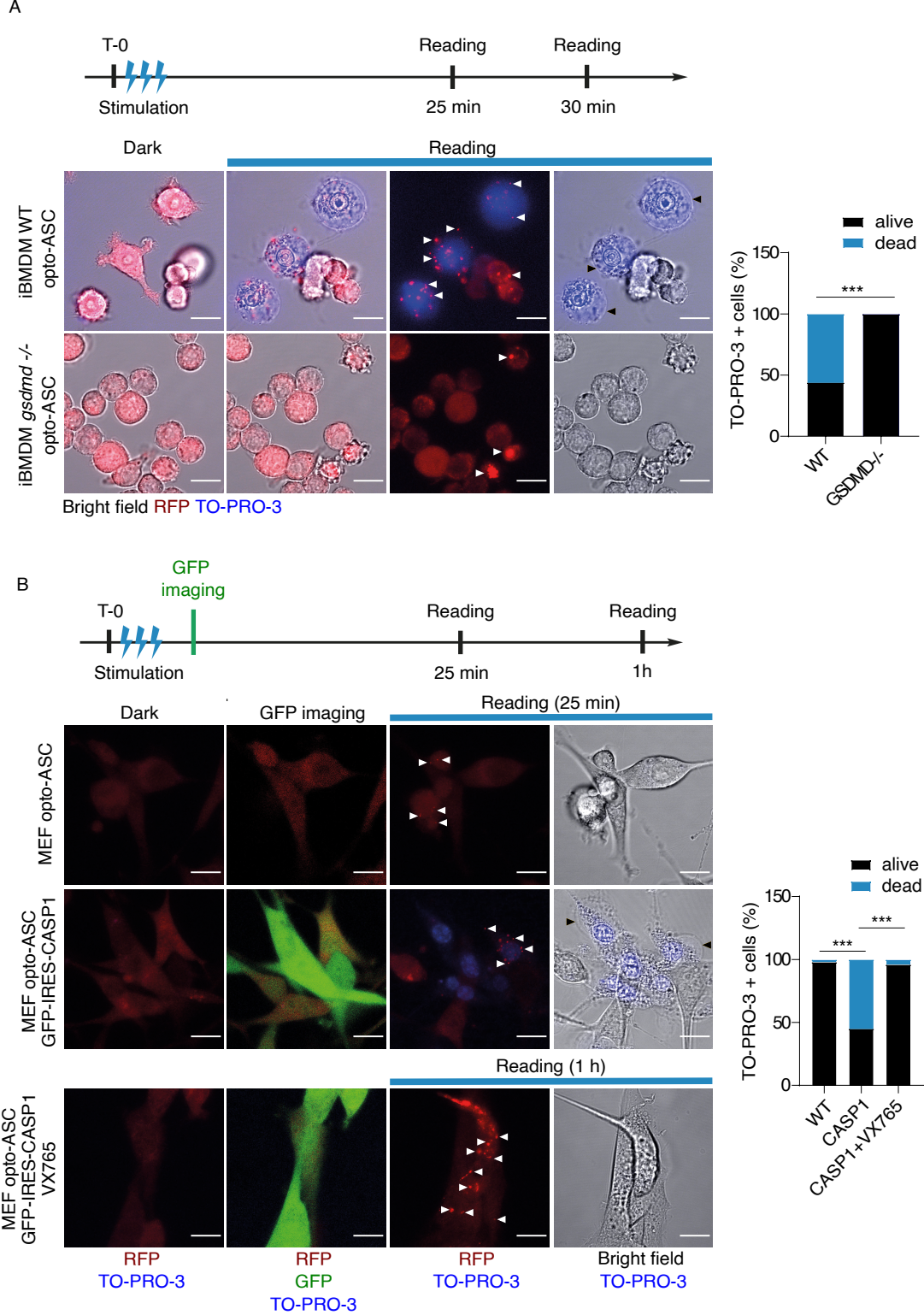

Nadjar et al. Figure 3

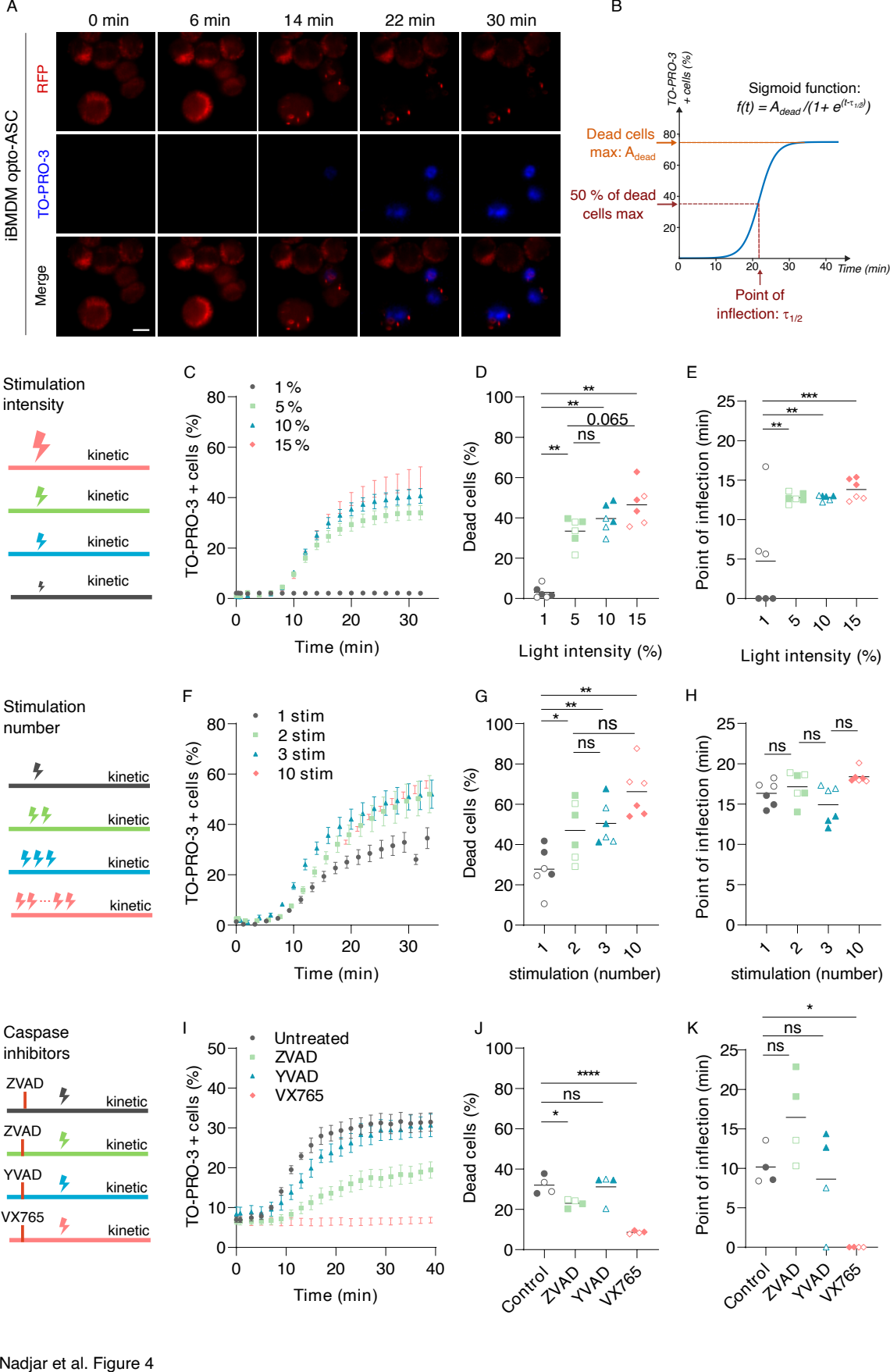

Nadjar et al. Figure 4

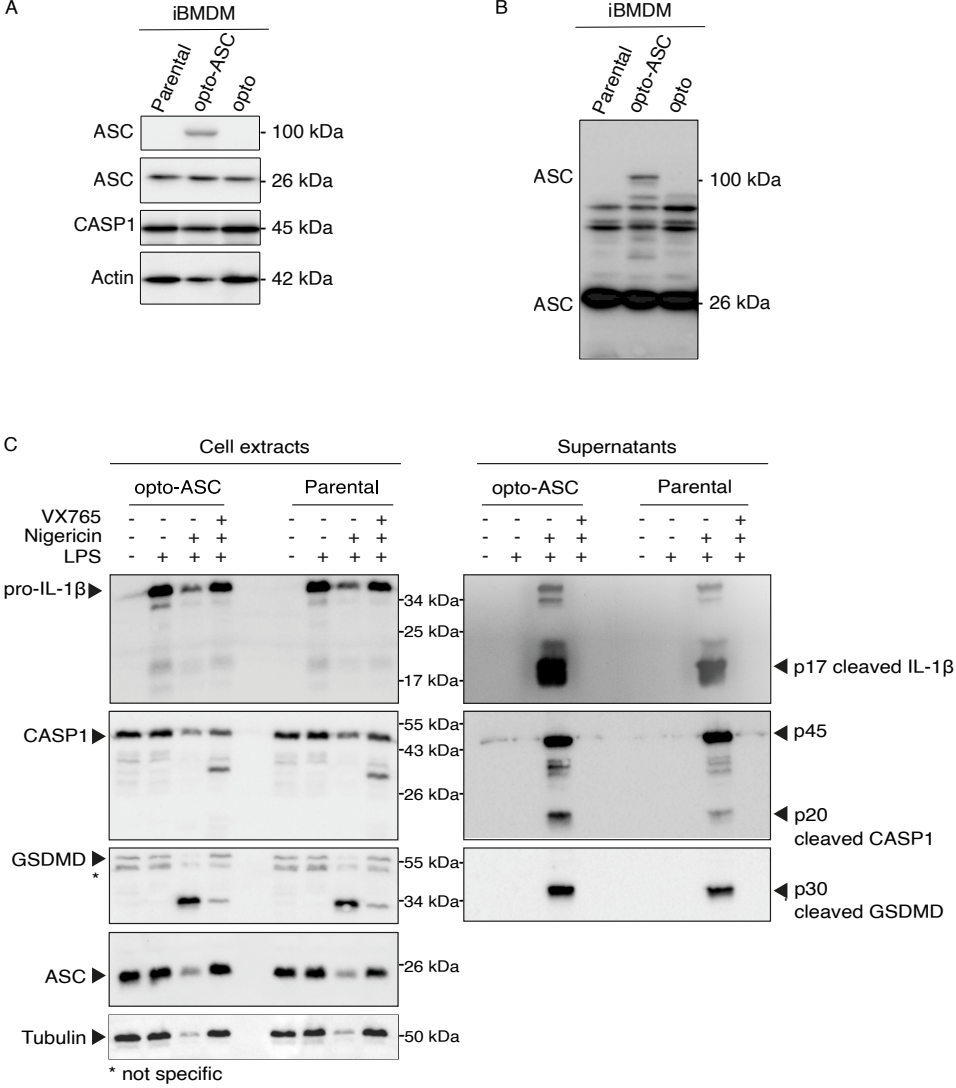

Nadjar et al. Supp Figure 1

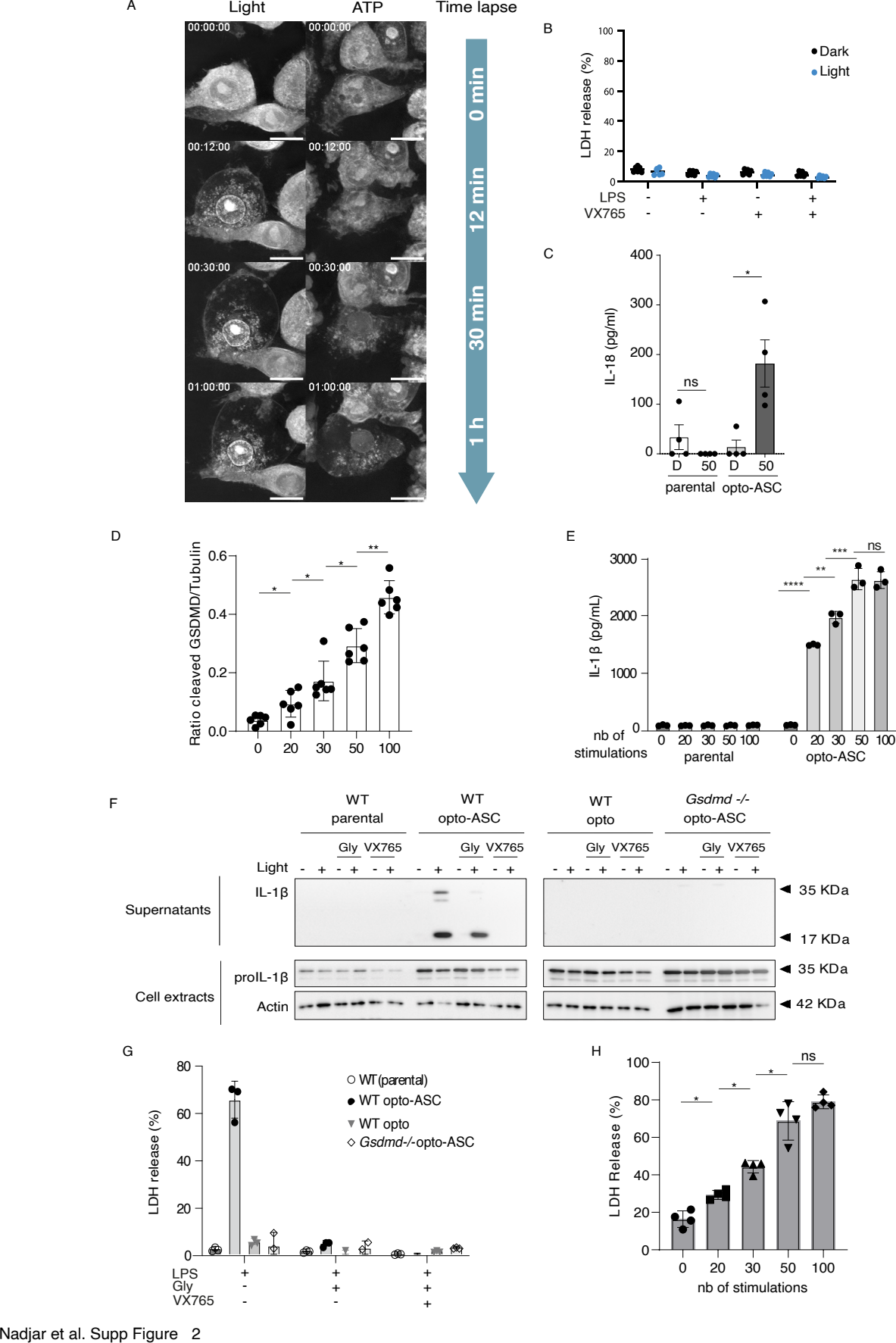

Nadjar et al. Supp Figure 2

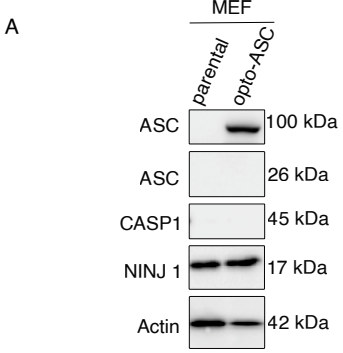
A
MEF
parental
opto-ASC
ASC
100 kDa
ASC
26 kDa
CASP1
45 kDa
NINJ 1
17 kDa
Actin
42 kDa

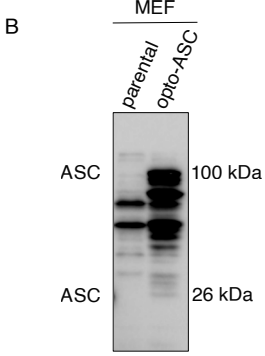
B
MEF
parental
opto-ASC
ASC
100 kDa
ASC
26 kDa

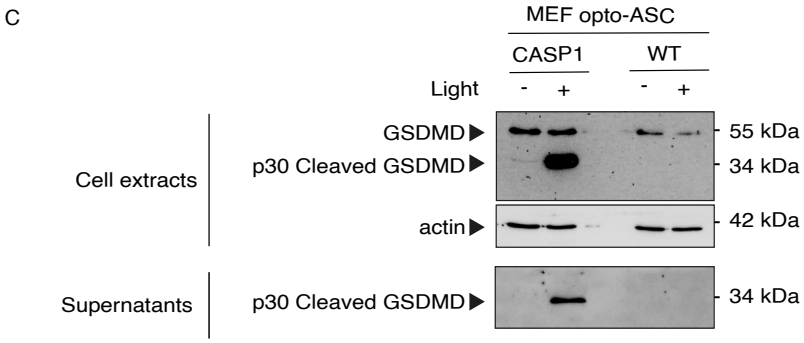
C
MEF opto-ASC
CASP1
WT
Light
-
+
-
+
Cell extracts
GSDMD
p30 Cleaved GSDMD
55 kDa
34 kDa
actin
42 kDa
Supernatants
p30 Cleaved GSDMD
34 kDa

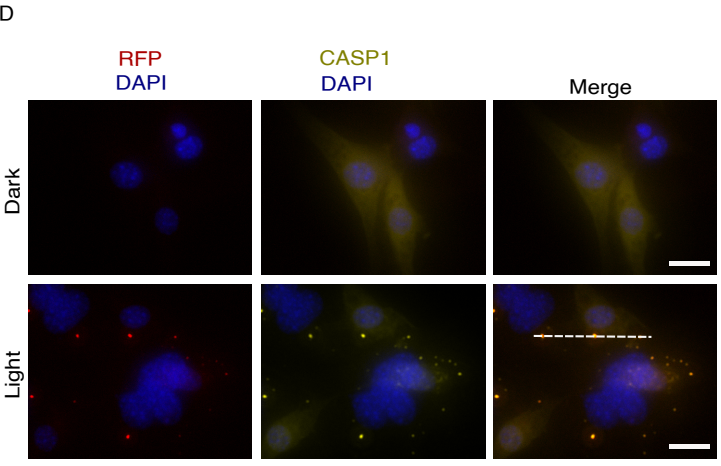
D
RFP
DAPI
CASP1
DAPI
Merge
Dark
Light

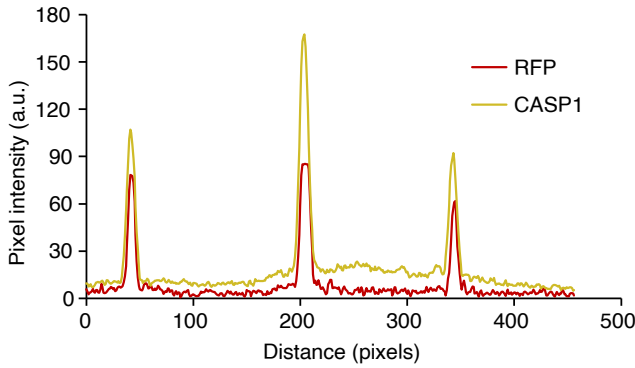
180
150
120
90
60
30
0
Pixel intensity (a.u.)
RFP
CASP1
0
100
200
300
400
500
Distance (pixels)

A

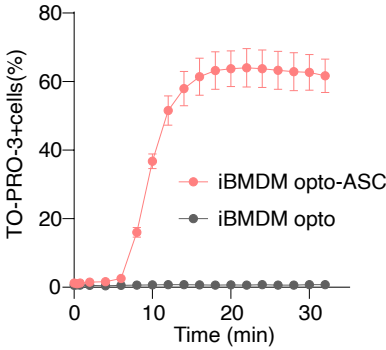
80
60
40
20
0
TO-PRO-3+cells(%)
0
10
20
30
Time (min)
iBMDM opto-ASC
iBMDM opto

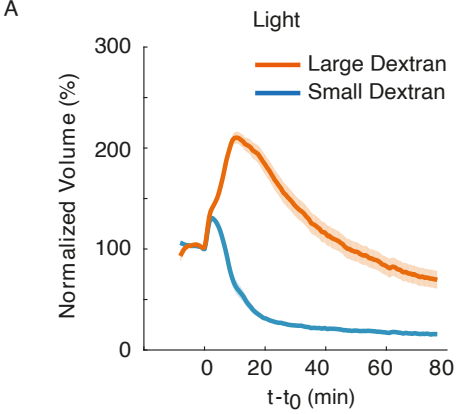
A
Light
Large Dextran
Small Dextran
Normalized Volume (%)
300
200
100
0
0
20
40
60
80
t-t0 (min)

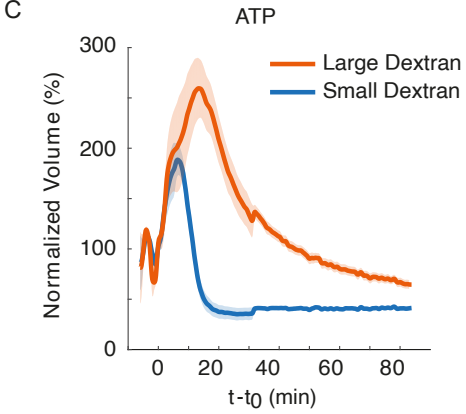
C
ATP
Large Dextran
Small Dextran
Normalized Volume (%)
300
200
100
0
0
20
40
60
80
t-t0 (min)

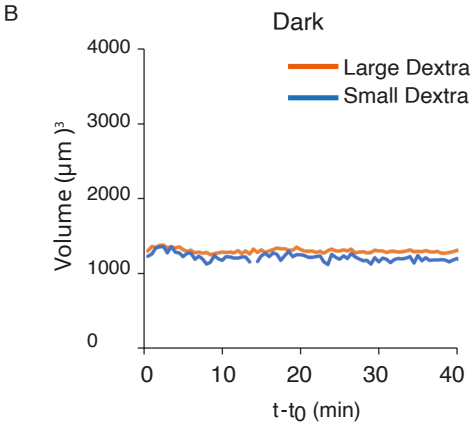
B
Dark
Large Dextran
Small Dextran
Volume (µm)3
4000
3000
2000
1000
0
0
10
20
30
40
t-t0 (min)

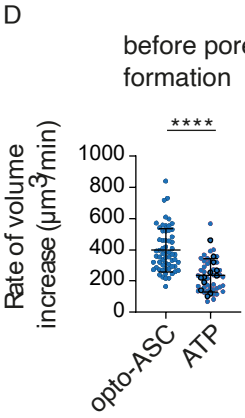
D
before pore formation
****
Rate of volume increase (µm3/min)
1000
800
600
400
200
0
opto-ASC
ATP

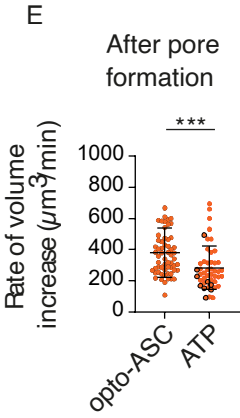
E
After pore formation
***
Rate of volume increase (µm3/min)
1000
800
600
400
200
0
opto-ASC
ATP

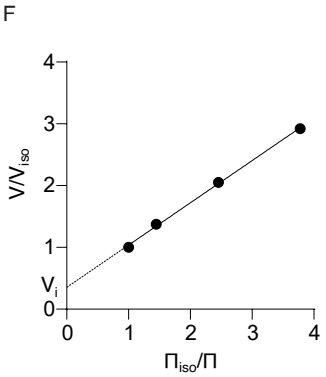
F
V/Viso
4
3
2
1
Vi
0
0
1
2
3
4
Πiso/Π